Thermal convection in rotating spherical geometry. A numerical overview of the transitions from periodic axisymmetric to temporally complex 3D flows

J. Sánchez Umbría[*] and M. Net[†]

Physics Department, Universitat Politècnica de Catalunya,

Jordi Girona Salgado 1–3, Campus Nord,

Mòdul B4, 08034 Barcelona, Spain

(Dated: December 20, 2022)

Abstract

The aim of this work is to elucidate the type of transitions that take place when the periodic axisymmetric flows, which can set up at the onset of thermal convection in rotating fluid spheres, lose stability, and to study the behavior of the new stable velocity fields until the flows become temporally chaotic. The computations for Prandtl numbers Pr=0.715, 0.1 and 0.01 show that when it decreases, the range of stability of these flows becomes narrower because the kinetic energy of the axisymmetric periodic solutions increases very fast, favoring their instability. From the stability analysis and direct 3D simulations it is found that the transition to stable quasiperiodic flows through Neimark-Sacker bifurcations is supercritical when Pr$\geq$ 0.01. For Pr=0.1 two branches of stable periodic flows emerging from the conduction state have been found due to the proximity to a double Hopf bifurcation. However, only the branches bifurcating from the azimuthal rotating waves are stable at large Rayleigh numbers. Far from this bifurcation the stable flows keep the influence of the axisymmetric dynamics up to large Rayleigh numbers. For small Pr they behave as repeated transients of mixed dynamics, controlled by the azimuthal wavenumbers $m = 0$, $m = 1$ and $m = 2$.

[*] juan.j.sanchez@upc.edu

[†] marta.net@upc.edu

I. INTRODUCTION

The knowledge of how the thermal convection develops in rotating spherical geometry is fundamental for the understanding of the dynamics of most of the fluid celestial bodies. The type of transitions that take place near the onset influence the kinetics, heat transfer and the generation of magnetic fields at the high supercritical regimes of planets and stars. Aside seismological and space-probe observations, and laboratory experiments [1, 2] one of the main sources of information continues to be numerical simulation. The list of numerical studies and authors working on this subject, and on the generation of magnetic fields from the seventies is so long that it is impossible to make a complete review in a few lines. Therefore, only recent publications closely related with the present study or introducing new phenomena to the most classic approach (Boussinesq approximation with perfectly conducting and non-slip boundaries) will be mentioned here. Most of the simulations are carried out in spherical shells with non-slip boundary conditions, motivated by the geometry of the Earth's core, focusing in the laminar and turbulent regimes [3–5]. The nonlinear numerical studies in full fluid spheres internally heated, either in non-slip or stress-free boundary conditions, are scarce [6–9] despite their interest in astrophysics. Much more unusual are the studies taking into account the flattening of the sphere due to fast rotation rates [10–13], as happens in some luminous stars.

For most of the parameter pairs (Prandtl, Pr, and Ekman, E, numbers) that can be chosen to integrate the equations describing the thermal convection in rotating spherical geometry, the onset of convection appears as an azimuthal rotating wave (ARW) [9, 14–16] because the rotational invariance of the conduction state is broken at the first bifurcation. These waves are symmetric with respect to the equator. However, in the region found in [8, 17–19] the first bifurcation keeps the invariance by axial rotations, and the transition gives rise to axisymmetric periodic (AP) oscillations, which are almost antisymmetric with respect to the equator. At low Pr, the instability is due to the Coriolis force and, consequently, the angular frequency of the oscillations is $\mathcal{O}(E^{-1})$. The range of parameters where these oscillations can arise from rest was fully determined in [20]. Near the onset the AP oscillations consist of a poloidal vortex, which fills the sphere and reverses its rotation every half period, and an azimuthal motion with opposite velocities in each hemisphere, which also changes its direction but with a phase shift relative to the poloidal field. When Ra increases this

velocity field gives rise to a latitudinal transport of the kinetic energy on the surface of the sphere in contrast to the ARWs. See Fig. 1 to visualize a typical periodic torsional flow.
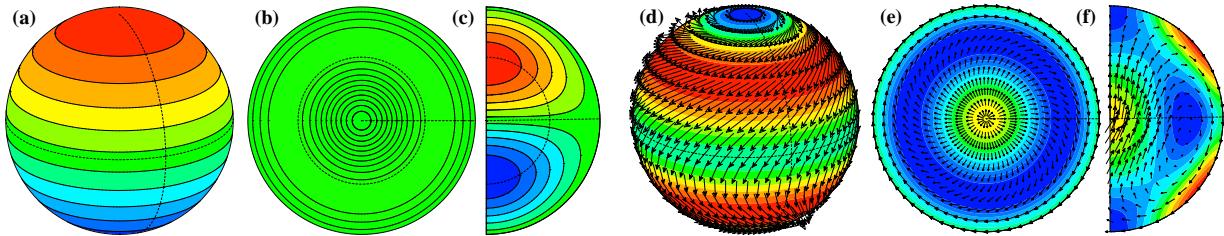

FIG. 1. Snapshots of the spherical, equatorial and meridional projections of (a)-(c) the perturbation of the temperature with respect the conduction state, and (d)-(f) the kinetic energy density (contour plots) together with the velocity field (arrows), for $Ra = 7.34 \times 10^3$ and Pr=0.01. The cut of each section is indicated in the other two.

A recent study [21] of the dynamics of the torsional flows at very low Pr showed that, when the axisymmetric flows bifurcated from the conduction state lose stability, the arising quasiperiodic (QP) flows start to drift in the azimuthal direction due to the breaking of the axisymmetry. Quasiperiodic oscillations were found at Pr=0.001 below the critical Rayleigh number, Ra, but the bifurcations were so close to each other, and the temporal integration transients were so long, that it was almost impossible to find out the nature of the bifurcations, and the origin of the dynamics observed. Therefore that study was mainly centered on the type of quasiperiodicity of the convective flows before temporal chaos arises. The objective of this study is to integrate the equations at larger Pr to obtain more information on the transitions between the large-scale flows of thermal convection, coming from periodic axisymmetric velocity fields in rotating fluid spheres, and their dependence with Pr.

A goal of this study is to ratify that the onset of the axisymmetric convection is supercritical for any Pr [8, 19], and to show that for Pr$\geq$ 0.01 the bifurcation leading to quasiperiodicity is also supercritical. Moreover, it also shows that this transition introduces the drift observed in the subsequent complex time dependent flows, and that it is not just due to the stabilization of branches of quasiperiodic ARWs. Only for Pr close to 0.1 does the drift of the flows at large Ra come from that of the periodic ARWs.

The rest of the article is organized as follows: After the introduction, Sec. II is devoted to briefly introduce the mathematical model. Section III describes the bifurcation diagrams

and dynamics of the flows obtained for three Pr< 1, and Sec. IV is a discussion and summary of the content.

II.   THE EQUATIONS

The dynamics in a rotating, self-gravitating, and internally and uniformly heated spherical shell is studied numerically by integrating the Boussinesq approximation of the mass, momentum, and energy equations. Constant rotation about the vertical axis, $\mathbf{\Omega} = \Omega \mathbf{k}$, and radial gravity proportional to the position vector, $\mathbf{g} = -\gamma \mathbf{r}$, are considered. The system is written in spherical coordinates, (r, θ, φ), (θ being the colatitude and φ the longitude) in the rotating frame of reference, and the centrifugal force is neglected because in many self-gravitating bodies $\Omega^2/\gamma \ll 1$. The length, time, and temperature are scaled with $d = r_o^* - r_i^*$, d^2/ν, and $\nu^2/\gamma\alpha d^4$, respectively. The dimensional quantities are the internal radius, r_i^*, the external, r_o^*, the kinematic viscosity, ν, and the thermal expansions coefficient, α.

The resultant non-dimensional divergence-free velocity field is written in terms of toroidal, Ψ, and poloidal, Φ, potentials as $\mathbf{v} = \mathbf{\nabla} \times (\Psi \mathbf{r}) + \mathbf{\nabla} \times \mathbf{\nabla} \times (\Phi \mathbf{r})$, and the energy equation in terms of the temperature perturbation, $\Theta^* = \mathrm{T}^* - \mathrm{T}_c^*$, from the temperature of the conduction state $\mathrm{T}_c^* = A + \frac{B}{r} + Cr^2$. The symbol T^* is used for full temperature. Since an objective of the work is to obtain more information about the convection in the fluid from the temporal integration of the equations in a shell of $r_i^* \approx 0$, and in the full sphere regularity conditions at $r = 0$ imply $B = 0$, the approximation $B = 0$ is taken in the wide shell. In this way the equations are written in both geometries for the same perturbation Θ^* of the same conduction state, which is then given by $\mathbf{v} = \mathbf{0}$ and $\mathrm{T}_c(r) = \mathrm{T}_0 - (\mathrm{Ra}/2\mathrm{Pr})r^2$, in non-dimensional form.

Then the system for Ψ, Φ and Θ becomes

$$(\partial_t - \Delta)\mathcal{L}_2\Psi = 2E^{-1}(\partial_\varphi\Psi - \mathcal{Q}\Phi) - \mathbf{r} \cdot \mathbf{\nabla} \times (\mathbf{\omega} \times \mathbf{v}), \tag{1}$$

$$(\partial_t - \Delta)\mathcal{L}_2\Delta\Phi = 2E^{-1}(\partial_\varphi\Delta\Phi + \mathcal{Q}\Psi) - \mathcal{L}_2\Theta + \mathbf{r} \cdot \mathbf{\nabla} \times \mathbf{\nabla} \times (\mathbf{\omega} \times \mathbf{v}), \tag{2}$$

$$(\mathrm{Pr}\,\partial_t - \Delta)\,\Theta = \mathrm{Ra}\,\mathcal{L}_2\Phi - \mathrm{Pr}\,(\mathbf{v} \cdot \mathbf{\nabla})\Theta. \tag{3}$$

The operators $\mathcal{L}_2$ and $\mathcal{Q}$ are defined as $\mathcal{L}_2 \equiv -r^2\Delta + \partial_r(r^2\partial_r)$, and $\mathcal{Q} \equiv r\cos\theta\Delta - (\mathcal{L}_2 + r\partial_r)(\cos\theta\partial_r - r^{-1}\sin\theta\partial_\theta)$, and $\mathbf{\omega} = \mathbf{\nabla} \times \mathbf{v}$ is the vorticity.

4

The parameters of the system are the Prandtl, Rayleigh and Ekman numbers

$$\mathrm{Pr} = \frac{\nu}{\kappa}, \quad \mathrm{Ra} = \frac{q\gamma\alpha d^6}{3c_p\kappa^2\nu}, \quad E = \frac{\nu}{\Omega d^2}. \tag{4}$$

The coefficients q, c_p, and κ are the rate of internal heat generated per unit mass, the specific heat at constant pressure, and the thermal diffusivity, respectively.

The stress-free, impenetrable ($v_r = 0$), and perfect thermally conducting boundary conditions, used here to close the problem, become

$$\Phi = \partial_{rr}^2\Phi = \partial_r(\Psi/r) = \Theta = 0 \quad \text{at} \quad r_i = \eta/(1-\eta) \quad \text{and} \quad r_o = 1/(1-\eta), \tag{5}$$

where r_i and r_o are the non-dimensional internal and external radii, respectively, and $\eta = r_i/r_o$ is the radii ratio, which will be taken very small. These boundary conditions require enforcing the conservation of the angular momentum in the domain during the temporal integration [8, 22, 23].

Details on some tests to check the accuracy of the temporal integrators can be found in [21]. Just mentioning that the functions were expanded in spherical harmonics of order m (azimuthal wavenumber) and degree l, Y_l^m, on the sphere, with $0 \leq |m| \leq l \leq L$, and a collocation method on a radial mesh of $N_r + 1$ Gauss-Lobatto points was used. All the computations have been done with $N_r = 48$ and $L = 64$. To dealiase the products the number of collocation nodes in longitude and colatitude are $N_\varphi = 196$ and $N_\theta = 98$, respectively. This resolution is enough to give very low relative errors. For instance, at Ra $= 14000$ and Pr$=0.1$, the averaged kinetic energy density (defined below) differs less than 1.5% from that using $N_r = 64$, $L = 80$, $N_\varphi = 256$ and $N_\theta = 128$.

Equations (1)-(3) with boundary conditions (5) are $\mathcal{SO}(2) \times \mathcal{Z}_2$-equivariant, with $\mathcal{SO}(2)$ generated by azimuthal rotations of an arbitrary angle φ_0, and $\mathcal{Z}_2$ by reflections with respect to the equatorial plane, i.e., the actions

$$R_{\varphi_0}: \quad (\Psi, \Phi, \Theta)(t, r, \theta, \varphi) \to (\Psi, \Phi, \Theta)(t, r, \theta, \varphi + \varphi_0), \quad \text{and} \tag{6}$$

$$\zeta_\theta: \quad (\Psi, \Phi, \Theta)(t, r, \theta, \varphi) \to (-\Psi, \Phi, \Theta)(t, r, \pi - \theta, \varphi), \tag{7}$$

leave the system invariant.

The dynamics of the flows is analyzed by monitoring the frequencies and global quantities such as the mean zonal flow and some kinetic energy densities. The zonal flow is defined as

$$\langle v_\varphi \rangle = \frac{1}{2\pi} \int_0^{2\pi} v_\varphi \, d\varphi, \tag{8}$$

5

and the kinetic energy density $k(t) = 1/2\,(\boldsymbol{v}(t) \cdot \boldsymbol{v}(t))$ is averaged over the whole volume of the sphere, V. This average, with the normalization of the spherical harmonics used, is

$$K(t) = \frac{1}{V} \int_V k(t, r, \theta, \varphi)\, dV = \frac{3\sqrt{2}}{4(r_o^3 - r_i^3)} \int_{r_i}^{r_o} r^2 [v^2]_0^0(t, r)\, dr, \tag{9}$$

where $[v^2]_0^0$ means the spherical harmonic coefficient of order and degree zero of v^2. The same expression can be used for computing the zonal (axisymmetric), $K_z(t)$, and non-zonal (non-axisymmetric), $K_{nz}(t)$, parts by replacing v by the corresponding component.

The temporal average of any of the above energies, $\overline{K}_*$ and of the zonal flow $\overline{\langle v_\varphi \rangle}$ over a time interval Δt are computed as

$$\overline{X} = \frac{1}{\Delta t} \int_0^{\Delta t} X\, dt. \tag{10}$$

From now on, the time and space averaged quantities will be called 'mean' for short.

The spectra of frequencies of the azimuthal component of the velocity field, $v_\varphi(t, r_o, \pi/6, 0)$, shown in this study, were calculated using Fast Fourier Transforms (FFTs), and the frequencies of highest amplitude also using Laskar's NAFF method (numerical analysis of fundamental frequencies) [24]. They were also computed for the values of some spherical harmonic coefficients at a radial point for checking purposes. In addition, projections of Poincaré sections, and a code giving any peak of the spectra of frequencies as the linear combination of those selected as fundamental, up to a given error, were used to help to distinguish the different types of solutions. Moreover, these relations are important since they are a confirmation that the temporal integration is sufficiently accurate.

III. DESCRIPTION AND ANALYSIS OF THE RESULTS

In order to clarify the bifurcation diagrams near the onset of the periodic axisymmetric convection, the nonlinear calculations were performed in a fluid shell of $\eta = 0.001$, with selected pairs (Pr,E)=$(0.715, 0.0475)$, $(0.1, 0.01)$, and $(10^{-2}, 10^{-3})$ falling inside the region of parameters where this type of convection appears [20]. The critical Rayleigh numbers and frequencies given by the linear stability analysis of the conduction state in a shell of the same η, using the techniques described in [17, 25], are $\mathrm{Ra}_c = 6.853 \times 10^3$ with frequency $f_{1c} = 1.774$ for Pr=0.715, $\mathrm{Ra}_c = 6.218 \times 10^3$ with frequency $f_{1c} = 13.23$ for Pr=0.1, and $\mathrm{Ra}_c = 7.329 \times 10^3$ with frequency $f_{1c} = 141.34$ for Pr=0.01. The frequencies f_{1c}, and the

6

corresponding eigenfunctions, agree very well with those given by the asymptotic analysis in a fluid sphere [18, 19], but Ra_c is a 0.5% below the value given by the theory. The same agreement in the critical frequencies and slight discrepancy in the critical Ra were already observed numerically in [18], and in [21] for $\eta = 0.01$ and Pr=0.001.

As a previous step, and in order to compare the results obtained in this study with those obtained for the fluid sphere (FS), and to recognize the second main frequency, f_2, of the quasiperiodic orbits bifurcated from the AP oscillations in the shell, the branches of AP solutions were recomputed in the FS with a continuation method [8]. The frequency, f_1^{FS}, of the AP orbits, and in particular that at the point where they lose the stability, is $f_1^{\text{FS}} = 1/T^{\text{FS}}$, where T^{FS} is the period obtained from the continuation method. Moreover, preliminary results on their stability against symmetry-breaking perturbations (those breaking the rotational invariance) show that the AP orbits destabilize through Neimark-Sacker bifurcations (Hopf bifurcation of periodic orbits, from now on NS). The critical frequencies f_{2c}^{FS} were obtained from the first Floquet multiplier crossing the unit circle, which gives the rotation number of the QP solution, ρ, and from the frequency of the orbit at the bifurcation point, f_1^{FS}, according to $f_{2c}^{\text{FS}} = (\rho/2\pi)f_1^{\text{FS}}$. Roughly speaking, ρ is a measure of the averaged angle rotated by the subsequent iterates of the Poincaré map. For a rigorous definition of ρ see for instance [26]. Critical parameters $Ra_c^{\text{FS}} = 8.0465 \times 10^3$ with $f_{2c}^{\text{FS}} = 0.3193$ for Pr=0.715, $Ra_c^{\text{FS}} = 6.7012 \times 10^3$ with $f_{2c}^{\text{FS}} = 2.985$ for Pr=0.1, and $Ra_c^{\text{FS}} = 7.4779 \times 10^3$ with $f_{2c}^{\text{FS}} = 29.197$ for Pr=0.01 were obtained from the stability analysis. In any of the cases the critical azimuthal wavenumber is $m_c^{\text{FS}} = 1$, breaking the invariance by azimuthal rotation of the AP orbits.

From now on, and for any sequence of bifurcations, subscript 1 refers to the frequency of a periodic orbit, subscript 2 refers to the second main frequency of a two-frequency quasiperiodic orbit, and subscript 3 refers to the third independent frequency of a three-frequency quasiperiodic orbit. As above, the subscript 'c' means the value at a critical point, and only parameters and values with the superscript FS refer to the full sphere. The symbol for the critical Rayleigh number for a second bifurcation on any branch of solutions is written inside parentheses with a subscript 2. For instance, $(Ra_c^{\text{FS}})_2$ means the second critical Ra computed on any branch in the case of a full sphere. Subscript 3 is used for the third bifurcation on any branch. For instance, $(Ra_c)_3$ means the third critical Ra on a branch in the case of a shell.
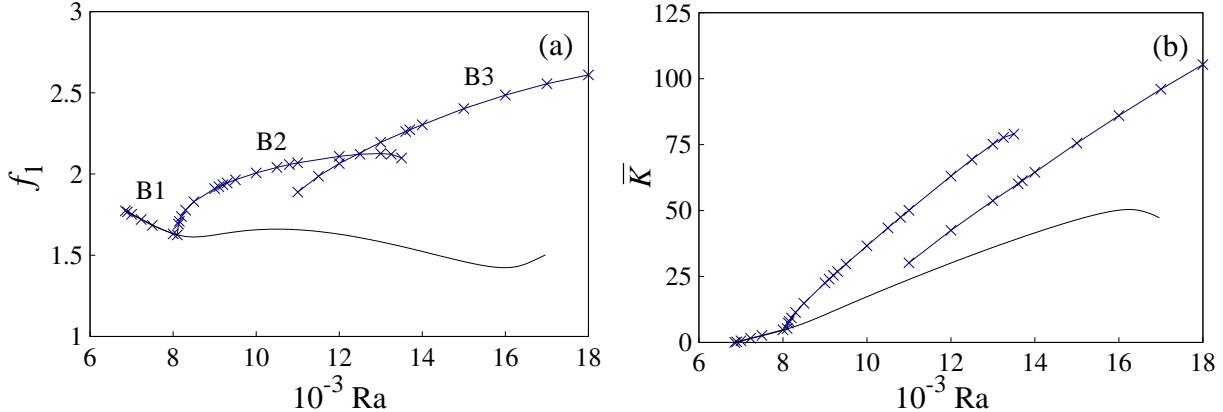
FIG. 2. (a) First fundamental frequency f_1 of the solutions versus Ra (blue crosses). (b) Mean kinetic energy density, $\overline{K}$ (blue crosses) for the same solutions. In both cases the solid black line is the branch of AP orbits computed for the fluid sphere with the same parameter Pr=0.715.

A. Pr=0.715

At Pr=0.715, which is an example of the largest Pr for which axisymmetric convection can set up as primary flow, the transitions are clearly separated, and it is relatively easy to understand the bifurcation diagram. Figure 2(a) shows the main frequency of the solutions, f_1, versus Ra, and Fig. 2(b) the mean full kinetic energy density, $\overline{K}$. The first (leftmost) symbol denotes the bifurcation point given by the stability analysis of the conduction state, mentioned before. The solid black line is the branch of AP orbits calculated by the continuation method in a FS (also mentioned before) for the same parameters [8]. The last symbol near the black solid branch indicates the point were the periodic orbits become unstable. The agreement between the stable AP solutions in the FS and a shell of small η is very good, as well as the critical points and frequencies where they lose stability.

The loss of stability of the AP orbits (solutions B1 in Fig. 2(a)) through a NS bifurcation takes place for Ra $\approx 8.1 \times 10^3$. Then a new supercritical branch of QP solutions (B2) is found. The bifurcation breaks the axisymmetry of the periodic orbits and the flow starts a retrograde drift in the azimuthal direction. It also introduces a fast increase of the mean non-zonal flow, $\overline{K}_{nz}$, while the mean zonal flow, $\overline{K}_z$, undergoes a slight decrease near the bifurcation point, and a moderate growth after (see Fig. 3).

To determine the frequency f_2 of the QP flows, we have compared the frequencies of

8

the Fourier spectra of the azimuthal component of the velocity field of these solutions at $r = 1.01$, $\theta = \pi/6$, and $\varphi = 0$, with that given by the stability analysis of the periodic orbit in the FS ($f_{2_c}^{\mathrm{FS}} = 0.3193$ for Pr=0.715, given above). This frequency matches with the lowest frequency of the spectrum of the QP solutions near the bifurcation point. For instance, at Ra $= 8.13 \times 10^3$, $f_2 = 0.3865$. However, the time $1/f_2$ is not observed in the animations of the solutions projected on the equatorial plane as happen at very low Pr [21]. In this case the flow drifts faster with frequency $f_D = 2.996$. The frequency f_D is the second highest peak in the spectrum of the velocity field near the transition (see Fig. 4(a)). Moreover, it has been checked that f_D is the frequency of largest amplitude of the time evolution of the spherical harmonic coefficient $\Phi_{l=1}^{m=1}(r)$, and f_2 the smallest and second in amplitude (purple curve in Fig. 4(a)). When Ra increases, f_D becomes soon the most important peak of the spectra of the velocity field, and the dynamics is dominated by the azimuthal drift with $k(t)$ concentrated around the poles and the center of the sphere. Then, there is no latitudinal transport of $k(t)$ as for very low Pr [8, 19], but Θ displays the interchange of the sign between hemispheres. The analysis of the frequencies of the Fourier spectrum of Fig. 4(a) has been carried out to confirm that B2 bifurcates from B1, and that the drifting does not stem from a second bifurcation from the conduction state. Since the QP orbit has frequency $f_1 = 1.691$ at Ra $= 8.13 \times 10^3$, it is clear that $f_D = 2f_1 - f_2$ with a relative error $\varepsilon = 2 \times 10^{-6}$. Consequently, the drifting frequency is related to the frequency of the AP because f_1 is 1.625 just before the bifurcation at Ra $= 8.1 \times 10^3$.

As can be seen in Fig. 4(b), all the Poincaré sections are closed curves, and then the flows computed remain QP, and stable up to Ra $\approx 1.35 \times 10^4$, where the invariant curve loses the smoothness and breaks down. The black plus in Fig. 4(b) is the section of an AP orbit near the bifurcation point to QP flows.

A jump to a new branch of QP solutions is found at Ra $= 1.35 \times 10^4$ when Ra is increased. This branch can be extended down to Ra $\approx 1.1 \times 10^4$, where $f_1 = 1.889$ and $f_2 = 0.521$. As can be seen from Figs. 2(b) and Fig. 3 it remains disconnected from the others branches, and $\overline{K}_{nz}$ quickly overcomes $\overline{K}_z$.

The stability analysis of the AP orbits in the FS shows that a second pair of multipliers crosses the unit circle at $(\mathrm{Ra}_c^{\mathrm{FS}})_2 = 1.139 \times 10^4$. At this point the frequency of the AP orbit is $f_1^{\mathrm{FS}} = 1.6492$, and the frequency given by the second multiplier crossing the unit circle is $(f_{2_c}^{\mathrm{FS}})_2 = 0.4209$. This frequency is close to $f_2 = 0.5208$, corresponding to the second largest

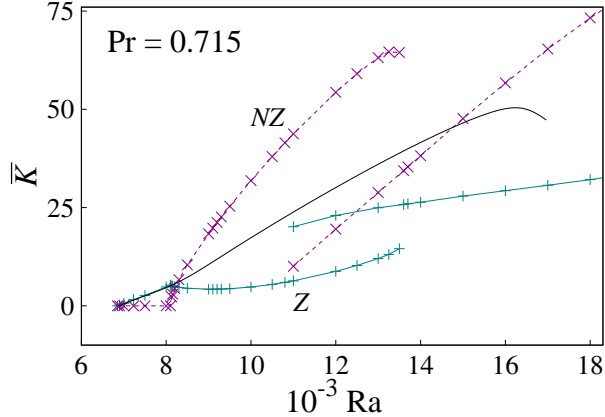FIG. 3. Mean zonal, $\overline{K}_z$, and non-zonal, $\overline{K}_{nz}$, kinetic energy densities versus Ra of the three branches of solutions for Pr=0.715. $\overline{K}_z$ is hown in teal solid lines with pluses, and $\overline{K}_{nz}$ in purple dashed lines with crosses. The solid black line shows $\overline{K}$ on the branch of AP orbits for the fluid sphere.

peak of the Fourier spectra of the velocity field of the QP orbits starting at Ra $\approx 1.1 \times 10^4$ (see the black curve in Fig. 5(a)), and to the largest of the perturbation (see the purple curve in the same figure). To understand the difference, it must be taken into account that at Ra $= 1.1 \times 10^4$ the branches B1 and B3 (see Fig. 2(a)) are at a certain distance and, in addition, the frequencies are computed for slightly different geometries. Therefore, it seems clear that the new branch comes from a second bifurcation on the branch of AP oscillations, which should be subcritical. The new QP flows are initially unstable but they soon stabilize. The slope of the curve B3 in Fig. 2 also points to this fact. Moreover, the second transition is also a symmetry-breaking bifurcation. In this case, f_2 approximates directly the frequency of the slow retrograde drift of the solutions. For these flows the drift is superposed to the latitudinal propagation of $k(t)$ giving rise to the local spot of $k(t)$, meandering on the surface of the sphere [21]. (See the animations for Ra $= 1.4 \times 10^4$ and a time interval $1/f_2$, Pr0.715-E0.0475-Ra1.4e4-ptem.gif and Pr0.715-E0.0475-Ra1.4e4-ener.gif [27]). However, in contrast to the flows of very low Pr, $k(t)$ is less localized on the surface, and there is also a transport of $k(t)$ around and through the center the sphere.

Note that for Pr=0.715 there coexist fast and slow QP waves, the azimuthal drifting time of the former being more than six times shorter than that of the latter. On the other hand, details of the Poincaré projections of Figs. 4(b) and 5(b) and the linear combinations of
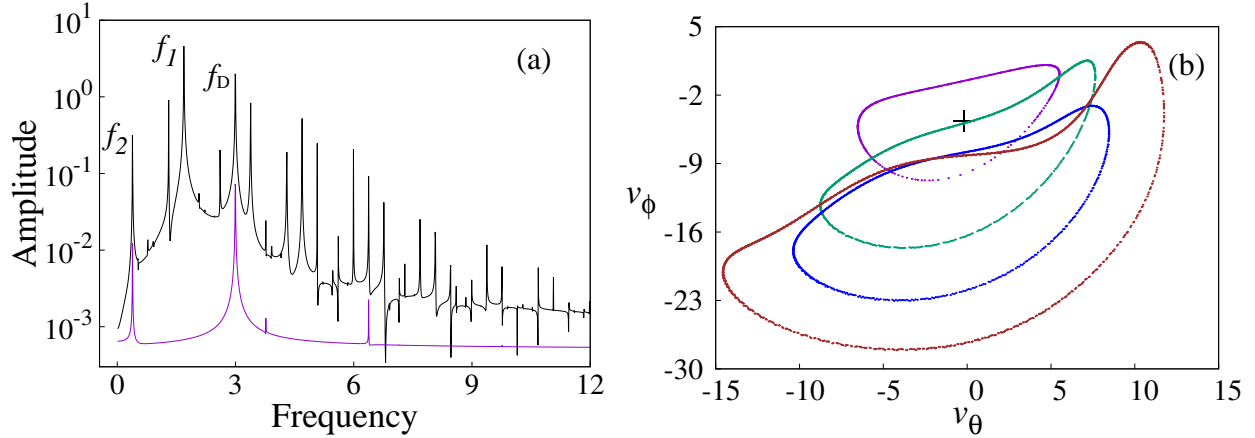
10

FIG. 4. (a) Fourier spectrum of $v_\varphi(1.01, \pi/6, 0)$ (black) and $\Phi_{l=1}^{m=1}(0.85)$ (purple) for a QP solution at Ra = 8130 for Pr=0.715, in logarithmic scale. (b) Projections of the Poincaré sections showing $v_\varphi(1.01, \pi/6, 0)$ versus $v_\theta(0.26, \pi/6, 0)$ on the hyperplane $v_r(0.26, \pi/6, 0) = -1$ for Ra = 8×10^3 (black plus), 8.2×10^3 (smallest purple curve), 9.3×10^3 (teal), 1.1×10^4 (blue), and 1.3×10^4 (largest brown curve).
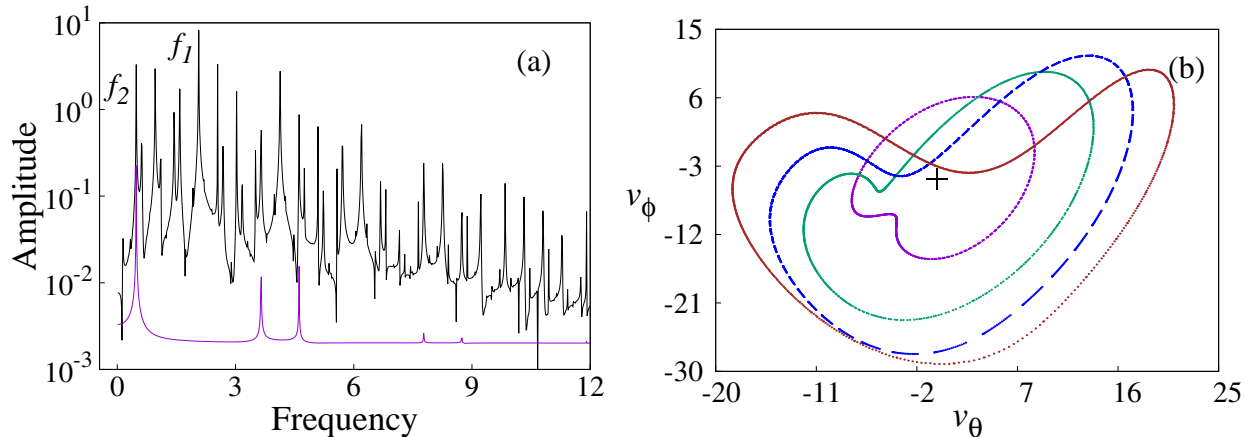
FIG. 5. (a) Idem Fig. 4(a) for Ra = 1.2×10^4 on the third branch, B3, of solutions. (b) Idem Fig. 4(b) for Ra = 8×10^3 (black plus), 1.1×10^4 (smallest purple curve), 1.3×10^4 (teal), 1.5×10^4 (blue), and 1.7×10^4 (largest brown curve).

the peaks of the Fourier spectra show that the flows may have either two or three main frequencies or may be resonant (frequency-locked) along the branches of QP solutions, as it happened in Ref. [21].
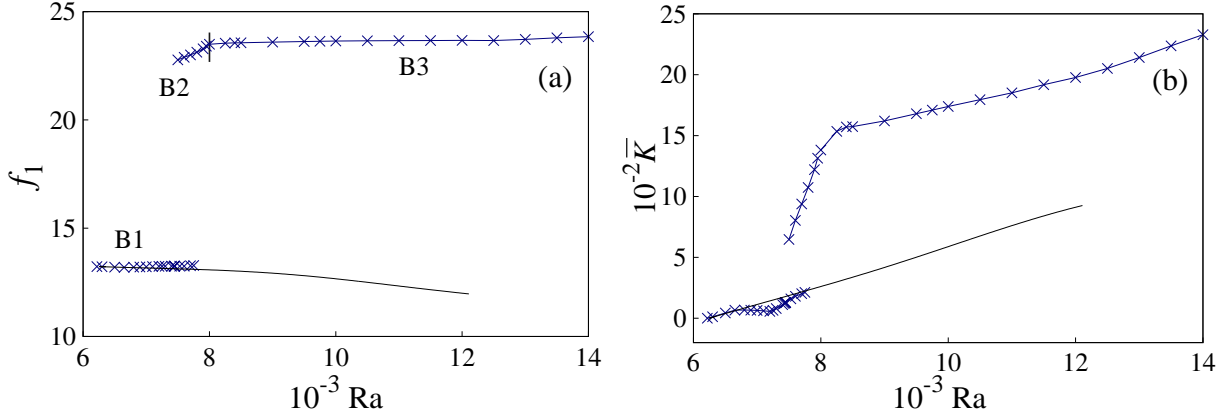
11

FIG. 6. Idem Fig. 2 for Pr=0.1.

B.   Pr=0.1

The stable flows found at Pr=0.1, shown in Figs. 6(a) and 6(b), differ substantially from those of the previous case. Three different sequences of solutions labeled B1, B2, and B3 were found. Each sequence has a different origin, and they are composed of solutions with different temporal dependence. They bifurcate successively from one another and are continuously connected, in each sequence. The term branch is only used when the solutions of a piece of a sequence have the same type of temporal dependence.

The first sequence B1 starts with the primary branch of AP flows. When it loses stability above $Ra = 6.65 \times 10^3$, a branch of prograde slow drifting QP solutions is found, due to the breaking of the axisymmetry. This transition is supercritical, and it is seen in the first change of slope of B1 in Fig. 6(b). The new frequency f_2 agrees very well with that given by the stability analysis of the AP solutions in the FS. For instance, at $Ra \approx 6.8 \times 10^3$ it is $f_2 = 2.963$. However, in contrast to what happen for Pr=0.715, the QP orbits soon undergo a transition to complex flows with the appearance of new independent frequencies. The new transition is also reflected in Fig. 6(b) with the second change of slope of B1, and in the change of the zonal flow in Fig. 7. The last complex solution directly related with the AP orbits was found at $Ra = 7.75 \times 10^3$. All these solutions maintain a small non-zonal contribution to $\overline{K}$ (see Fig. 7).

The Poincaré sections of the solutions (see Fig. 8) were analyzed to clarify the temporal dependence. It was found that at $Ra = 7.2 \times 10^3$ the two-dimensional projection of the
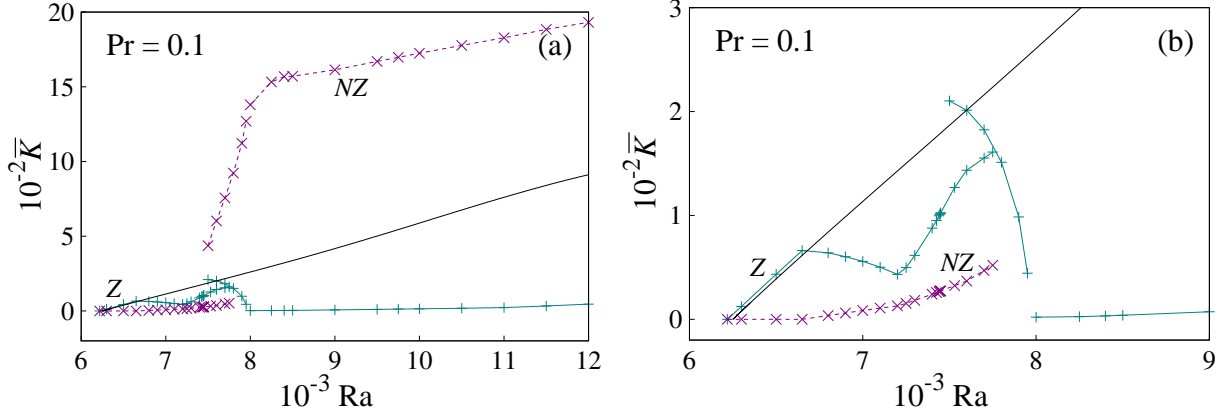
12

FIG. 7. (a) Idem Fig. 3 for Pr=0.1. (b) Detail of (a) at low Ra

Poincaré section is a closed curve, and at 7.25×10^3 it fills an area with a small frequency $f_3 = 0.574$. From 7.4×10^3 up to the end of the branch the trajectories become more entangled but they maintain the three-frequency quasi-periodicity.

The contour plots of the solutions show the interchange of sign of the perturbation of the temperature between the hemispheres, but notably modulated by the azimuthal wavenumber $m = 1$ from the beginning. The kinetic energy displays the typical superposition of the latitudinal motion and azimuthal drift of the torsional solutions at the breaking of the axisymmetry, but k is concentrated at the poles and around the center of the sphere as for Pr=0.715 at large Ra. The velocity field forms a strong jet pointing consecutively northward and southward through the center in the meridional section. (See the animations for Ra $= 6.8 \times 10^3$ and a time interval $1/f_2$, Pr0.1-E0.01-Ra6.8e3-ptem.gif and Pr0.1-E0.01-Ra6.8e3-ener.gif [27]).

For larger parameter values a new sequence of solutions, B3, was detected. Periodic fast azimuthal rotating waves (ARWs) of wavenumber $m = 1$ were found from Ra $\approx 8.0 \times 10^3$. At this point the main frequency of the wave is $f_1 = 23.492$, and it gives rise to a retrograde drift. The new solutions are related to the ARWs that bifurcate from the conduction state, since their frequency matches the second critical frequency, $(f_{1c})_2 = 22.423$, given by the stability analysis of the conduction state in the shell, at the second bifurcation point $(\text{Ra}_c)_2 = 6.467 \times 10^3$, which is very close to the first. In this case the rotational invariance is broken from the beginning by perturbations of azimuthal wavenumber $m = 1$, explaining the fast drift. Before this second transition the first two eigenvalues in crossing the imaginary axis still
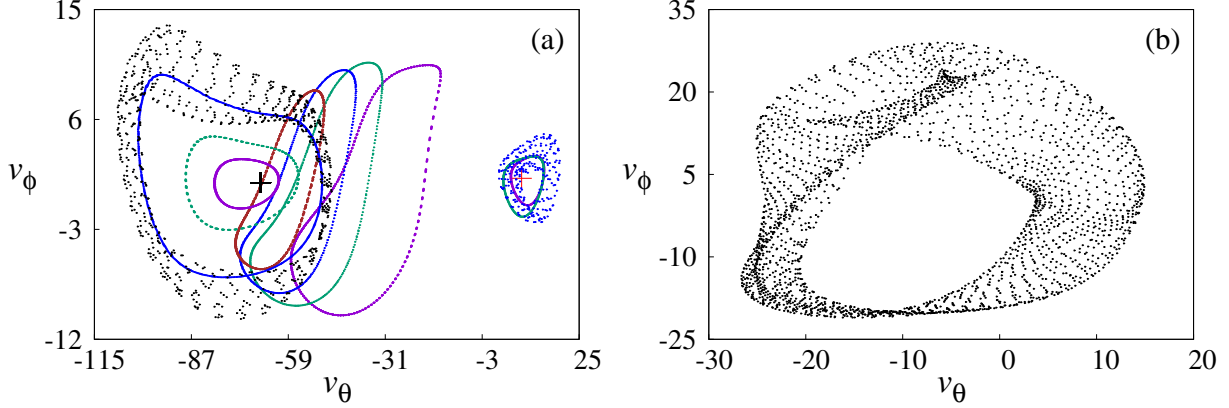
13

FIG. 8. (a) Going from right to left, projections of the Poincaré section showing $v_\varphi(0.76, \pi/6, 0)$ versus $v_\theta(0.26, \pi/6, 0)$ on the hyperplane $v_\varphi(1.01, \pi/6, 0) = 0$ for Ra = 6500 (red plus), 7000 (purple curve), 7200 (teal curve), 7300 (blue area), 7500 (big purple curve), 7700 (teal), 7800 (blue), 7900 (brown), 8000 (black plus), 8500 (left small purple curve), 9000 (teal), 10500 (blue), and 11000 (black area). (b) Same projection as in (a) on the hyperplane $v_\varphi(0.26, \pi/6, 0) = 1$ for Ra = 7750.
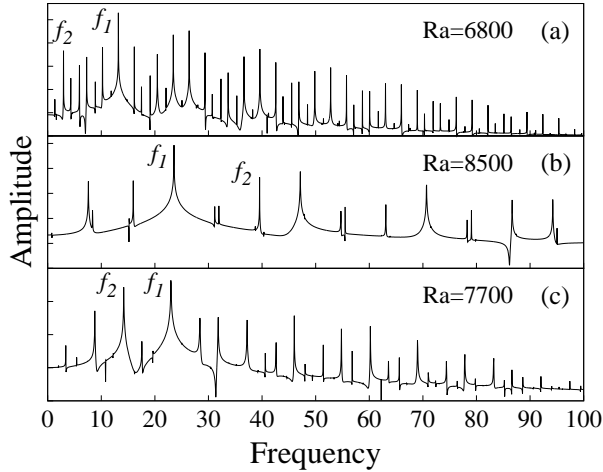

FIG. 9. Fourier spectra of the three types of two-frequency QP solutions found at Pr=0.1, in logarithmic scale.

have positive real part, and therefore the branch arising from $(\mathrm{Ra}_c)_2$ is initially unstable. It could be either sub or supercritical, but it is plausible that it stabilizes about $\mathrm{Ra} = 8.0 \times 10^3$.

The branch of periodic ARW undergoes a NS bifurcation before $\mathrm{Ra} = 8.4 \times 10^3$, and a branch of QP flows is found (see the change of slope of the upper branch of blue crosses in Fig. 6(b) and Fig. 7(a)). However, the frequency f_1 remains almost constant. This

14

bifurcation gives rise to the oscillation of the $m = 0$ spherical harmonic coefficients, which were constant before. This fact allows the identification of the new independent frequency f_2 of the quasiperiodic ARWs by computing the Fourier spectrum of the coefficients. For instance, at Ra $= 8.5 \times 10^3$, shown in Fig. 9, $f_1 = 23.561$ and $f_2 = 39.532$. As a confirmation that this f_2 triggers the quasi-periodicity, it was checked that all the peaks in the frequency spectrum may be written as linear combinations of f_1 and f_2. For instance, the peak of small frequency in the spectrum of the solution is $f = 2f_1 - f_2$, with a relative error $\varepsilon < 10^{-6}$. The energy $\overline{K}$ of the ARWs and bifurcated QP orbits is much higher than that of the first sequence B1. The main contribution is due to $\overline{K}_{nz}$, while that of $\overline{K}_z$ is almost negligible (see Fig. 7(a)). Then, from the secondary transition $\overline{K}$ increases due to the increase in $\overline{K}_{nz}$ as in B1.

Concerning the dynamics of the QP flows, the velocity field on a meridional section has two vortices with an oscillating horizontal jet through the center of the sphere. The maxima of k remain concentrated at the center and poles, and they never travel in latitude. A new low frequency f_3 appears between 1.05×10^4 and 1.1×10^4 when Ra increases, which generates three-frequency QP solutions. Finally, the flow becomes temporally chaotic when Ra $> 1.1 \times 10^4$. Therefore the ARWs and bifurcated solutions, directly connected with the conduction state, become the stable flows at large Ra.

For Pr=0.1 a third sequence of stable solutions between Ra $\approx 7.5 \times 10^3$ and 7.95×10^3 was found by decreasing Ra from the periodic ARWs (B2 in Fig. 6(a)). The new flows have two main frequencies, the first f_1, whose value fits that of the ARWs, and which is also linked to the retrograde azimuthal drift of the solution, and the second, f_2, whose value matches that of the AP oscillations (see Figs. 6(a) and 9). Therefore, B3 is probably bifurcated from these waves. For instance, at Ra $= 7.5 \times 10^3$, $f_1 = 22.774$ and $f_2 = 13.836$, with amplitudes of the same order, but with f_1 being always slightly higher. In addition, Fig. 7 shows that these solutions have $\overline{K}_z$ and $\overline{K}_{nz}$ of similar order at Ra $\approx 7.5 \times 10^3$, but $\overline{K}_{nz}$ increases quickly with Ra and $\overline{K}_z$ decreases, both energies approaching that of the ARWs when Ra $\approx 7.95 \times 10^3$. Moreover, the animations of $k(t)$ (not included) show that the dynamics is very complex. It is possible to distinguish the azimuthal and latitudinal traveling of the spots of $k(t)$, but in a random way. In addition, there is also a transfer of energy from the external surface to the interior of the shell. The presence of both frequencies, the diagram of energies, and the dynamics of the solutions seem to indicate that this is a mixed branch of solutions, linking
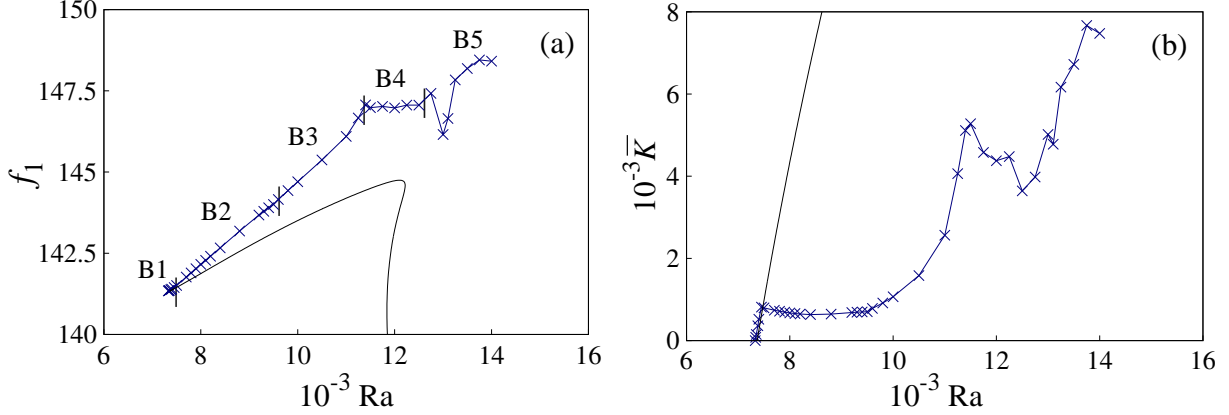
15

FIG. 10. Idem Fig. 2 for Pr=0.01.

those coming from the axisymmetric flows with the ARWs.

The differences among the three sequences found at low Ra and Pr=0.1 are shown in Figs. 8 and 9. The former shows the Poincaré projections illustrating the evolution of the solutions on each sequence. The small projections at right are those of the first sequence, connected with the conduction state (B1). Figure 8(b) shows the same projection of a different section of the last of these solutions, because with the previous it was difficult to see that at Ra $= 7.75 \times 10^3$ the Poincaré section is still concentrated around a closed curve. Those at left in Fig. 8(a) belong to the QP orbits bifurcated from the periodic ARWs, one of them indicated by the black plus, and the large curves in the middle to the mixed branch of QP orbits. Figure 9 shows the difference between the Fourier spectra of the three types of stable two-frequency QP solutions found. The upper row of the panel corresponds to the spectrum of a flow bifurcated from the AP orbits (B1). It is more complex than the others despite the proximity to the onset of convection. That in the middle is the spectrum of a QP rotating wave bifurcated from the periodic ARWs (B3), and the lower is that of a mixed solution (B2), with the frequency f_1 matching that of the ARWs, and f_2 that of the AP orbits.

C.   Pr=0.01

At the lowest Pr explored, and like in the case of a FS (see black solid line in Fig. 10(b)), the slope of $\overline{K}$ versus Ra is very steep, and the AP flows are stable in a tiny interval
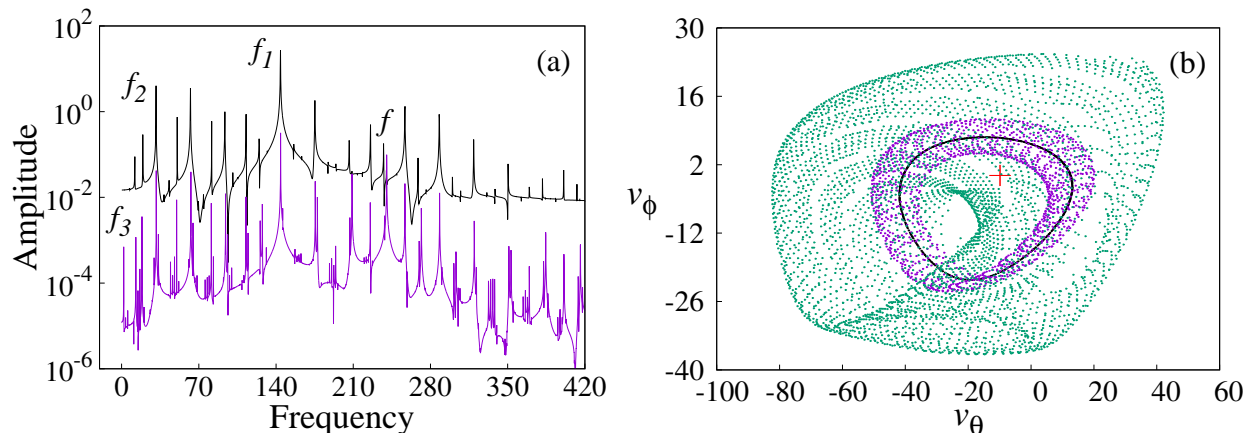
16

FIG. 11. (a) Fourier spectra of the QP solutions at Ra = 9500 (black) and 9600 (purple) for Pr=0.01 in logarithmic scale. (b) Projections of the Poincaré section showing $v_\varphi(0.76, \pi/6, 0)$ versus $v_\theta(0.26, \pi/6, 0)$ on the hyperplane $v_\varphi(1.01, \pi/6, 0) = 0$ for Ra = 7340 (red plus), 9500 (black curve), 9600 (purple area), and 10500 (teal).

(B1). They lose stability in a NS bifurcation, breaking the rotational invariance, around Ra = 7.45×10^3. The branch of QP solutions, starting there with two frequencies, is shown in the segment B2 of Fig. 10(a) and in Fig. 10(b). The second fundamental frequency, f_2, was obtained as before by comparing the Fourier spectra of frequencies with $f_{2_c}^{\rm FS}$, given by the linear stability analysis of the AP orbits in the FS. For instance, the matching frequency is $f_2 = 29.208$ at Ra = 7.5×10^3, and it introduces a prograde azimuthal drift to the solution. In this case $1/f_2$ gives the approximated drifting time observed on the equatorial plane.

The dynamics of these QP flows is very similar to that described in [21] for Pr=0.001, keeping a clear torsional motion superposed to the azimuthal drift. Concerning the kinetic energy, the transition to QP flows leads to a decrease of $\overline{K}$ up to a new transition to three-frequency QP flows at Ra $\approx 9.6 \times 10^3$. The purple curve of Fig. 11(a) is the Fourier spectrum of the solution very near to this point. The third linearly independent frequency is initially $f_3 = 1.922$. However, by comparing the spectra of the solutions before and after the change (see the black spectrum on the same figure), an increase in the amplitude of the peak of frequency $f = 240.34$ was found, passing from being small to the second in amplitude.

Moreover, to confirm the existence and the correct selection of the third independent frequency, the linear combinations of the frequencies of the main peaks of the spectrum were calculated. In particular, the relation $f = f_1 + 3f_2 + f_3$, with $f_1 = 144.15$, $f_2 = 31.419$,
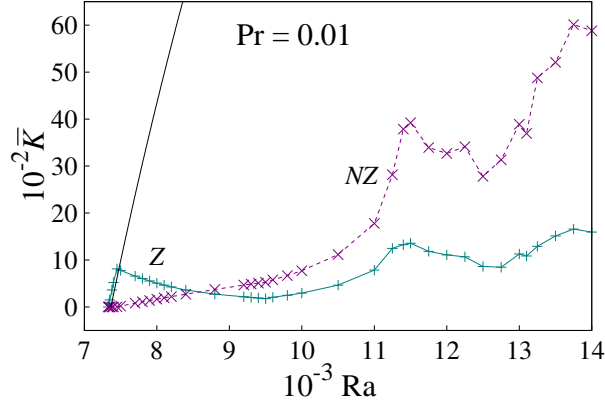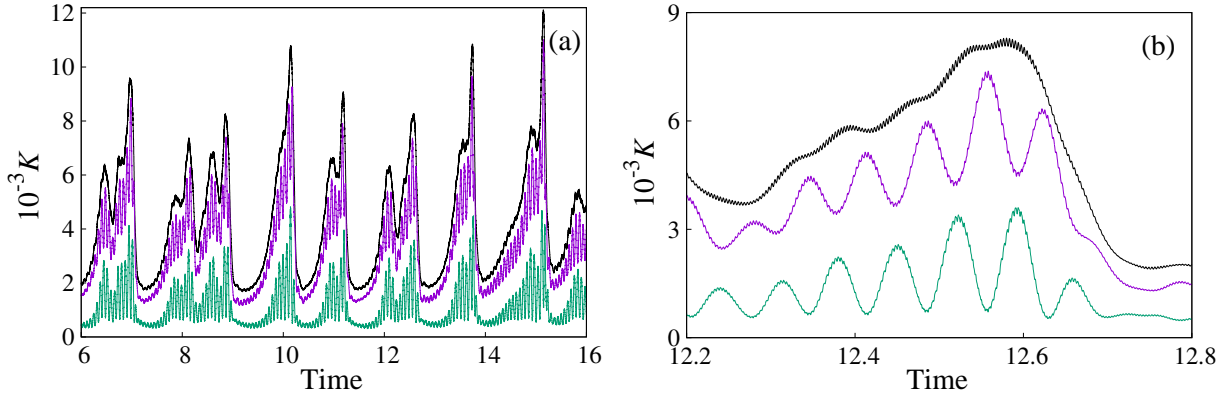
17

FIG. 12. Idem Fig. 3 for Pr=0.01.

FIG. 13. (a) Time evolution of the space-averaged energies of an intermittent solution: $K(t)$ (black highest curve), $K_z(t)$ (lowest teal), and $K_{nz}(t)$ (middle purple) for Pr=0.01 and Ra = 12000. (b) Detail of (a).

$f_3 = 1.922$, and relative error $\varepsilon = 10^{-5}$ was found for the peak of $f = 240.34$. Another confirmation of the three-frequency quasi-periodicity is given by the Poincaré section, which goes from being a closed curve to fill an area around the curve in the transition (see Fig. 11(b)). In the interval B3 the solutions have just three main frequencies. The growth of the weight of the harmonics of order $m = 1$ in the flow is reflected in the fast increase of $\overline{K}$ due to the increase of both $\overline{K}_z$ and $\overline{K}_{nz}$ from the appearance of the third frequency (see Figs. 10(b) and 12).

A stability analysis, computed for the shell, shows that the conduction state undergoes a second Hopf bifurcation at $(\mathrm{Ra}_c)_2 = 7.797 \times 10^3$ with frequency $(f_{1c})_2 = 238.55$ for
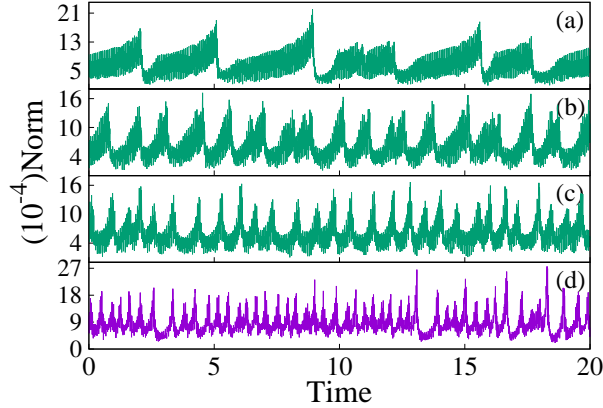
18

FIG. 14. $\mathcal{L}^2$ norms of the solutions found at (a) Ra = 1.14×10^4, (b) Ra = 1.2×10^4, (c) Ra = 1.25×10^4 while $\overline{K}$ is decreasing, and (d) Ra = 1.35×10^4 while $\overline{K}$ increases again. Pr=0.01.

perturbations of azimuthal wavenumber $m = 1$. Then, according to [19] the growth of the peak could be related with the initially unstable curve arising from the steady branch, originating a curve of mixed solutions when intersecting the QP torsional branch. This curve would be branch C in [19] despite the value of $\overline{K}$ differs in a factor. The difference is due to the stress-free boundary conditions used, because $\overline{K}$ depends on the value of the angular momentum at the beginning of the integration. Here it is set and maintained fixed to zero at any time. However, stable periodic ARWs were not found for Pr=0.01 by decreasing Ra. When it is increased the spectra of the solutions indicate that the growth of the above mentioned peak goes on, and at Ra = 1.1×10^4 it is already that of the highest amplitude.

The animations of the flows show a prograde drift on the surface of the sphere with approximate frequency f_2. However, the spot of $k(t)$ elongates longitudinally and splits during the motion; one of the spots disappears while the other goes forward at mid latitudes following a parallel (see the animations at Ra = 1.1×10^4, Pr0.01-E0.001-Ra1.1e4-ptem.gif and Pr0.01-E0.001-Ra1.1e4-ener.gif [27]).

When Ra is increased further, the appearance of smaller new frequencies about Ra = 1.14×10^4 leads to a temporal complex dynamics consisting of oscillations that increase the amplitude slowly and quasi-periodically, to recover suddenly the amplitude of the QP orbits in a cyclic way (B4). When this happens there is a fast decrease of $\overline{K}$ (see Fig. 12), and the time evolution of $K(t)$ shows repeated transients that evolve with a superposed fast low-amplitude oscillation (see Fig. 13). The total energy is not much larger than $K_{nz}(t)$

19

because the high amplitude oscillations of $K_z(t)$ and $K_{nz}(t)$ are out of phase, indicating an interchange between them. In any case, these large oscillations cancel out each other and, consequently, they are absent in the total energy $K(t)$. (see Fig. 13(b)). Moreover, $\overline{K}$ depends on the integration interval considered because the transients are very irregular.
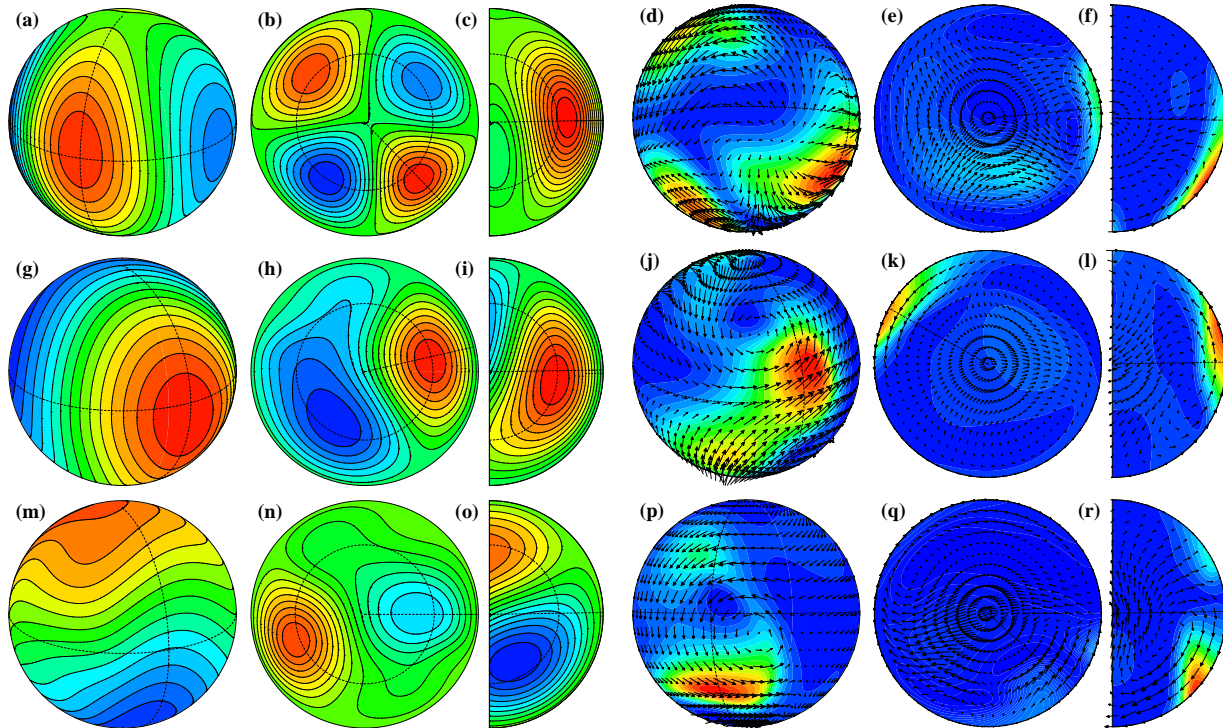

FIG. 15. Snapshots of the spherical, equatorial and meridional projections of Θ (first three columns) and of $k(t)$ and $\boldsymbol{v}$ (second three columns) at: (a)-(f) $t = 5.00$, the azimuthal wavenumber $m = 2$ is dominant, (g)-(l) $t = 8.22$, $m = 1$ is dominant, and (m)-(r) $t = 12.65$, $m = 0$ is dominant. In each case the sections are taken to show the maxima clearly. $Ra = 1.4 \times 10^4$ and Pr=0.01.

The period of the transients becomes shorter as Ra grows and $\overline{K}$ decreases. Figures 14(a)-(d), show the $\mathcal{L}^2$ norm of the solutions for several Ra. Finally, $\overline{K}$ starts to increase again at about $Ra = 1.25 \times 10^4$ (B5) (see Fig. 12), reaching the highest values at the end of the range computed. This change matches with the growth of the frequencies of the spherical harmonic $m = 2$, and it is clearly reflected in the behavior of the flow. For these solutions the peaks of the Fourier spectra of the spherical harmonic coefficients of azimuthal wavenumbers $m = 0$, $m = 1$ and $m = 2$ are of similar amplitude, being larger those of $m = 2$. The contour plots of Θ and k in Fig. 15 show that these flows behave as dominated by one of these harmonics as

20

time goes on, but most of the time by that of $m = 2$. However the influence of the torsional motion is recognized in the animations by the latitudinal traveling of the spots of $k(t)$. It has been checked that the changes in the dynamics are also reflected in the curve of the mean zonal flow, $\overline{\langle v_\varphi \rangle}$, versus Ra (not shown). At Ra $\approx 1.1 \times 10^4$, $|\overline{\langle v_\varphi \rangle}|$ starts to decrease up to Ra $\approx 1.15 \times 10^4$, while the dynamics displays the long transients of Fig. 14(a). When they become shorter, $|\overline{\langle v_\varphi \rangle}|$ increases, and finally, from Ra $\approx 1.25 \times 10^4$ it decreases again when the dynamics of the flow shows the influence of the spherical harmonics of azimuthal wavenumber $m = 2$.

Finally, the stability analysis of the conduction state for perturbations of $m = 2$ was undertaken to try to find an explanation of their weight in the dynamics of the flows in B5. It was found that the instability takes place at $(\text{Ra}_c)_3 = 1.253 \times 10^4$ with frequency $(f_{1c})_3 = 194.04$, which agrees well with the peak $f = 192.54$ of the harmonic $m = 2$ at Ra $= 1.25 \times 10^4$, so the final increase of $\overline{K}$ could be related with the interaction of the branch B4 with the unstable branch of $m = 2$ ARWs, arising unstable from the basic steady state, as could happen before with the $m = 1$ perturbations.

IV. DISCUSSION AND CONCLUSIONS

The thermal convection arising from AP flows (torsional) in a rotating wide spherical shell of radius ratio $\eta = 0.001$, heated uniformly from the interior, has been studied for three values of Pr. They cover from gases to liquid metals, and fall in the region of parameters inside which, according to [20], the onset of convection is to periodic axisymmetric oscillations. This region was computed for a fluid sphere, also with stress-free velocity boundary conditions, tracing the curves of double-Hopf points by continuation methods. It was found that it is bounded by the double-Hopf curves for the simultaneous bifurcations to azimuthal wavenumbers $(m_1, m_2) = (0, 1)$ when Pr < 0.9, and $(0, 2)$ close to Pr $= 0.9$. Moreover, it was also seen there that at low Pr the condition for the onset of axisymmetric convection fulfills very well the ratio Pr$/E = \mathcal{O}(10)$.

In this study, it is found that a shell of very small η approximates very well the critical Ra and frequency of the onset of the axisymmetric oscillations in a fluid sphere, and also the dynamics of the AP flows. It also gives a good approximation of the critical point where these flows lose their stability. When Pr decreases, the region of stability of the AP

21

flows becomes smaller because the kinetic energy grows very fast. In the cases studied, the critical Ra of the primary and secondary bifurcations in both geometries differ less than 1%. Moreover, if the secondary bifurcation is supercritical (as it happens in the cases studied) the dynamics of the emerging QP flows in the full sphere can be inferred, close to their onset, from that of the nonlinear solutions in the shell, and from the critical eigenfunction at the secondary transitions in the fluid sphere. In the latter case, the QP orbits should be a perturbation of the AP orbits, so the velocity field of a QP solution should be close to $v_{QP}^{FS} = v_{AP}^{FS} + \varepsilon\, v_{eigen}^{FS}$. From the animations of v_{QP}^{FS} and v_{QP}^{shell}, we have seen that the shell gives a good approximation of the QP dynamics, by selecting a suitable ε. However, below some value $\mathrm{Pr} < 0.01$, the transition from AP orbits to QP flows should be subcritical, since stable QP flows of wavenumber $m = 2$ were found in [21] below the secondary transition, and this argument cannot be applied.

The nonlinear QP and temporally chaotic dynamics, which arise when the AP flows lose stability, was investigated for a liquid metal of Pr=0.001 in a rotating shell of $\eta = 0.01$ [21], and also by setting Pr=0.01 and $\eta = 0.001$ [19], with the same configuration. Both studies displayed a good agreement concerning the stability of the AP flows, but the purely torsional QP solutions found in the former study were not found in the latter, and stable ARWs found in the latter were not found in the former. The extreme low Pr used in the first work implied to have very large relaxation times of integration that limited the number of solutions computed, and, in addition, a large number of transitions between different types of flows accumulated near the onset. The present study has analyzed the dynamics with different Pr larger than 0.001 in order to try to understand these discrepancies, and to find out in which range of parameters a dynamics influenced by the torsional motion at moderate Ra (twice the critical value) is maintained.

The full sphere was approximated with a shell of $\eta = 0.001$ to have exactly the geometry selected in [19]. The results indicate that the dynamics is extremely dependent on Pr, since this parameter determines the distance of the first and second transitions from the conduction state to a double-Hopf bifurcation point, from which simultaneous branches of AP oscillations and ARWs arise. For Pr=0.01 the critical Rayleigh numbers of the two first bifurcations from the conduction state are $\mathrm{Ra}_c = 7.329 \times 10^3$ giving rise to stable AP oscillations (torsional motion), and $(\mathrm{Ra}_c)_2 = 7.797 \times 10^3$ giving rise to unstable ARWs of azimuthal wavenumber $m = 1$, since when the real part of the second pair of eigenvalues

becomes positive, that of the first in crossing remains positive. It was checked that the ARWs are unstable (at least around the critical point $(Ra_c)_2$) by means of long temporal integrations of system (1)-(3) with initial conditions satisfying $Y_l^{m=1} \neq 0$ and $Y_l^{m\neq 1} = 0$. The fact that long integrations were needed to destabilize these waves is an indication that they are only slightly unstable. However, since the solutions found in the temporal integration of a nonlinear system are dependent on the initial conditions it is possible that they stabilize at higher Ra, and they were found in [19], and not in this study. In any case, their influence on the dynamics is seen at large Ra in the mixed solutions of the branch B3 in Fig. 2 and C in [19].

For Pr=0.01 no sign of hysteresis was found by increasing and decreasing Ra (at least with the increments of Ra used) when the slope of the curves changes. Moreover, the spectra show continuity of the frequencies, and although from $Ra > 1.1 \times 10^4$ the main frequencies of the spherical harmonic coefficients of $m = 1$ and $m = 2$ become as (or even more) important as those of $m = 0$, the influence of the torsional dynamics can still be observed in the movies. The temporal evolution of the contour plots of $k(t)$ and $\Theta(t)$ at the largest Ra studied show that the meandering motion of the spots on the surface of the sphere is modified due to the interaction with other branches of non-axisymmetric solutions. This interaction originates the generation and decay of new cells of convection, giving rise to a complex temporal dependence, but maintaining the frequency, f_2, of the drift. Since no hint of nearby heteroclinic orbits is found, the solutions of temporal complex dynamics seem to belong to mixed branches. This 3D complex flows with sudden variations of the velocity field are very good candidates to generate strong bursting magnetic fields as those found in [28] with an axisymmetric velocity field, although there the trajectory was a nearly heteroclinic chain, approaching and moving away from two unstable periodic orbits.

For Pr=0.1 the distance between the AP and ARW branches of oscillations is smaller than for Pr=0.01. The first bifurcation takes place at $Ra_c = 6.218 \times 10^3$ and the second at $Ra_c = 6.466 \times 10^3$. The proximity of both transitions leads to an increase of the complexity of the bifurcation diagram, and to the multiplicity of stable flows was found. In particular, stable pure ARWs were also detected with our temporal integration, so fast and slow quasiperiodic drifting waves coexist near the onset of convection. However, at large Ra only the flows bifurcated from the ARWs remain stable. Consequently the velocity field is nearly symmetric with respect to the equator and there is no latitudinal kinetic energy transport.

When Pr= 0.715 the distance between the two bifurcations is also larger than for Pr=0.1, and no hint of interaction of the two branches of oscillations was found. The first bifurcation takes place at $Ra_c = 6.852 \times 10^3$ and the second at $Ra_c = 7.188 \times 10^3$. In this case, two branches of QP solutions, both bifurcated from the AP orbits, coexist in a wide range of Ra. Then at large Ra the observed flows come from transitions of the axisymmetric states. However, the dynamics cannot be described like, in [21], as almost the composition of a latitudinal oscillation and an azimuthal drift. The spot of kinetic energy on the surface of the sphere $(r = r_o)$ is much less confined, and there is also a concentration of kinetic energy around the center of the sphere $(r = r_i$ in this case).

The preceding results, and those previously found in [19, 21] indicate that far from the double-Hopf bifurcation, giving rise simultaneously to branches of AP oscillations and ARWs, the initial bifurcation to axisymmetric flows has a deep influence on the subsequent dynamics at higher Ra. For large and low Pr the rotating flows bifurcated from the AP oscillations drift much slowly than those which break the invariance by rotation of the conduction state from their onset, usually found when $Pr/E \neq \mathcal{O}(10)$ [25, 29], and than those whose Pr is about 0.1, as seen in this study. The torsional dynamics is clear when Pr is large, and a remnant of the latitudinal oscillations is already seen at small Pr. Moreover, the comparison of the dynamics of the three Pr studied also shows that the concentration of $k(t)$ in the center of the sphere is larger when Pr is large, being nearly absent at very low Pr. The influence of the primary latitudinal oscillations on the turbulent flows at very high Ra remains to be analyzed.

DATA AVAILABILITY STATEMENT

The data that support the findings of this study are available from the corresponding author upon reasonable request.

[1] N. Gillet, D. Brito, D. Jault, and H.-C. Nataf, "Experimental and numerical studies of convection in a rapidly rotating spherical shell," J. Fluid Mech. **580**, 83–121 (2007).

[2] M. M. Adams, D. R. Stone, D. S. Zimmerman, and D. P. Lathrop, "Liquid sodium models of the Earths core," Progress in Earth and Planetary Science **2:29**, 1–18 (2015).

[3] S. Liu, Z.-H. Wan, R. Yan, C. Sun, and D.-J. Sun, "Onset of fully compressible convection in a rapidly rotating spherical shell," J. Fluid Mech. **873**, 1090–1115 (2019).

[4] C. Guervilly, P. Cardin, and N. Schaeffer, "Turbulent convective length scale in planetary cores," Nature **570**, 368–371 (2019).

[5] R. S. Long, J. E. Mound, C. J. Davies, and S. M. Tobias, "Scaling behaviour in spherical shell rotating convection with fixed-flux thermal boundary conditions," J. Fluid Mech. **889**, A7–1–32 (2020).

[6] C. Guervilly and P. Cardin, "Subcritical convection of liquid metals in a rotating sphere using a quasi-geostrophic model," J. Fluid Mech. **808**, 61–89 (2016).

[7] E. J. Kaplan, N. Schaeffer, J. Vidal, and P. Cardin, "Subcritical Thermal Convection of Liquid Methals in a Rapidly Rotating Sphere," Phys. Rev. Lett. **119**, 094501–1 (2017).

[8] J. Sánchez Umbría and M. Net, "Torsional solutions of convection in rotating fluid spheres," Phys. Rev. Fluids **4**, 013501 (2019).

[9] Y. Lin and A. Jackson, "Large-scale vortices and zonal flows in spherical rotating convection," J. Fluid Mech. **912**, A46 (2021).

[10] K. Zhang, X. Liao, and P. Earnshaw, "On inertial waves and oscillations in a rapidly rotating fluid spheroid," J. Fluid Mech. **504**, 1–40 (2004).

[11] K. H. Chan, X. Liao, and K. Zhang, "Simulations of fluid motion in spheroidal planetary cores driven by latitudinal libration." Phys. Earth Planet. Inter. **187**, 404–415 (2011).

[12] D. J. Ivers, "Tilted incompressible Coriolis modes in spheroids," J. Fluid Mech. **833**, 131–163 (2017).

[13] G. Backus and M. Rieutord, "Completeness of inertial modes of an incompressible inviscid fluid in a corotating ellipsoid," Phys. Rev. E **95**, 053116, pp16 (2017).

[14] K. Lam, D. Kong, and K. Zhang, "Nonlinear thermal inertial waves in rotating fluid spheres," Geophys. Astrophys. Fluid Dyn. **112**, 357–374 (2018).

[15] T. T. Clart, N. Schaeffer, S. Labrosse, and J. Vidal, "The effects of a robin boundary condition on thermal convection in a rotating spherical shell," J. Fluid Mech. **918**, A36 (2021).

[16] K. Lam, D. Kong, and K. Zhang, "Localised thermal convection in rotating spheres that undergo weak precession," Geophys. Astrophys. Fluid Dyn. **115**, 280–296 (2021).

[17] J. Sánchez, F. Garcia, and M. Net, "Critical torsional modes of convection in rotating fluid spheres at high Taylor numbers," J. Fluid Mech. **791**, R1 (2016).

[18] K. Zhang, K. Lam, and D. Kong, "Asymptotic theory for torsional convection in rotating fluid spheres," J. Fluid Mech. **813**, R2 (2017).

[19] D. Kong, K. Zhang, K. Lam, and A. P. Willis, "Axially symmetric and latitudinally propagating nonlinear patterns in rotating spherical convection," Phys. Rev. E **98**, 031101(R) (2018).

[20] J. Sánchez Umbría and M. Net, "Continuation of Double Hopf Points in Thermal Convection of Rotating Fluid Spheres," SIAM J. Appl. Dyn. Syst. **20**, 208–231 (2021).

[21] J. Sánchez Umbría and M. Net, "Three-dimensional quasiperiodic torsional flows in rotating spherical fluids at very low Prandtl numbers," Phys. Fluids **33**, 114103 (2021).

[22] B. Durney, "Convective Spherical Shell: II. With Rotation," J. Atmos. Sci. **25**, 771–778 (1968).

[23] P. S. Marcus, "Stellar convection. I. Modal equations in spheres and spherical shells." Astrophys. J. **231**, 176–192 (1979).

[24] J. Laskar, "Introduction to frequency map analysis," in *Hamiltonian Systems with Three or More Degrees of Freedom*, edited by C. Simó (Springer Netherlands, Dordrecht, 1999) pp. 134–150.

[25] M. Net, F. Garcia, and J. Sánchez, "On the onset of low-Prandtl-number convection in rotating spherical shells: non-slip boundary conditions," J. Fluid Mech. **601**, 317–337 (2008).

[26] Y. A. Kuznetsov, *Elements of Applied Bifurcation Theory* (Springer, Berlin, 1998).

[27] See Supplemental Material at `http://link.aps.org/supplemental/***` for animations of the temperature perturbation, energy and velocity field for several sets of parameters.

[28] J. Sánchez Umbría and M. Net, "Generation of bursting magnetic fields by nonperiodic torsional flows," Phys. Rev. E **100**, 053110 (2019).

[29] E. Dormy, A. M. Soward, C. A. Jones, D. Jault, and P. Cardin, "The onset of thermal convection in rotating spherical shells," J. Fluid Mech. **501**, 43–70 (2004).